Analytical and numerical modelling of the Swift effect in elastoplastic torsion

L. Gambirasio, P. Chiodi, E. Rizzi*

Università di Bergamo, Facoltà di Ingegneria, Dip.to di Progettazione e Tecnologie, viale G. Marconi 5, I-24044 Dalmine (BG), Italy

***Contact Author, fax: +39.035.205.2310, email: egidio.rizzi@unibg.it

ABSTRACT. *Torsion tests are widely used to investigate the elastoplastic behaviour of metallic materials, particularly when large strains are involved, up to the specimen's fracture. Such tests induce multiaxial inhomogeneous stress/strain and damage fields into the specimen. In this paper, elastoplastic torsion at room temperature of uniform isotropic circular solid and tubular metallic specimens is investigated in the finite strain range, both in analytical and numerical forms. The paper reports preliminary results of an on-going research project at the University of Bergamo [1]. Particular emphasis is given to the evaluation of the so-called Poynting (in the elastic domain) and Swift (in the plastic range) effects [2,3], i.e. the recorded axial length variation of the specimen that may appear under free-end torsion.*

INTRODUCTION

The analytical investigation has been carried-out within the elastic range and just for the case of fixed-end torsion, both for tubular and solid specimens, by assuming a priori a kinematic field for the response of the torsion specimen. Special attention is given to the outcomes that arise from the adoption of three different objective stress rates, namely Cotter-Rivlin, Truesdell and Jaumann-Zaremba stress rates, particularly when large strains are involved. The numerical investigation is carried-out for the whole torsion test, up to fracture separation, for both tubular and solid specimens and for both fixed- and free-end conditions, taking into consideration several hardening models and a damage model. Numerical results are based and compared with data available in [4].

ANALYTICAL RESULTS

A kinematic field for the specimens under fixed-end torsion is assumed, which applies to both solid and tubular specimens. Because of the axisymmetry of the specimen, a cylindrical coordinate system is adopted. Upper case letters (R, Θ, Z) denote the initial radial, angular and longitudinal coordinates at any point of the specimen, gathered in

vector $\mathbf{Y}^{\mathrm{T}} = \{\mathrm{R}, \Theta, \mathrm{Z}\}$. Conversely, lower case letters (r,θ,z) and vector $\mathbf{y}^{\mathrm{T}} = \{\mathrm{r}, \theta, \mathrm{z}\}$ denote the corresponding current coordinates.

The twist angle at the generic cross-section is denoted by α and is assumed to be a linear function of time t and longitudinal coordinate Z:

$$\alpha(\mathrm{Z}, \mathrm{t}) = \beta(\mathrm{t})\mathrm{Z} = \dot{\beta}\mathrm{t}\mathrm{Z}\,, \tag{1}$$

where $\beta(\mathrm{t})$ is the twist angle per unit initial length, with assumed constant time derivative $\dot{\beta}$. The longitudinal coordinate z(**Y**,t) is assumed to remain always equal to its initial value Z; this hypothesis is inspired by the condition of fixed-end torsion and automatically copes with it. For the sake of simplicity, it is also assumed that the specimen deforms (elastically) at constant volume. Thus, the radial coordinate r(**Y**,t) also keeps equal to its initial value R. The current angular coordinate θ(**Y**,t) can be expressed in the form $\theta(\mathbf{Y}, \mathrm{t}) = \Theta + \alpha = \Theta + \dot{\beta}\mathrm{t}\mathrm{Z}$. According to all made assumptions, the kinematic field can be resumed as follows:

$$\begin{cases} \mathrm{r}(\mathbf{Y}) = \mathrm{R} \\ \theta(\mathbf{Y}, \mathrm{t}) = \Theta + \dot{\beta}\mathrm{t}\mathrm{Z} \\ \mathrm{z}(\mathbf{Y}) = \mathrm{Z} \end{cases} . \tag{2}$$

By denoting with $\gamma = \beta\mathrm{R}$ the shear strain field (axisymmetric and linear in R) and with $\dot{\gamma}$ its time derivative, it is possible to derive, from the kinematic field (2), the expressions of deformation gradient **F**, velocity deformation gradient $\mathbf{L} = \mathbf{D} + \mathbf{W}$, rate of deformation **D** and spin tensor **W**:

$$[\mathbf{F}] = \begin{bmatrix} 1 & 0 & 0 \\ 0 & 1 & \gamma \\ 0 & 0 & 1 \end{bmatrix}, \quad [\mathbf{L}] = \begin{bmatrix} 0 & 0 & 0 \\ 0 & 0 & \dot{\gamma} \\ 0 & 0 & 0 \end{bmatrix}, \quad [\mathbf{D}] = \begin{bmatrix} 0 & 0 & 0 \\ 0 & 0 & \frac{\dot{\gamma}}{2} \\ 0 & \frac{\dot{\gamma}}{2} & 0 \end{bmatrix}, \quad [\mathbf{W}] = \begin{bmatrix} 0 & 0 & 0 \\ 0 & 0 & \frac{\dot{\gamma}}{2} \\ 0 & -\frac{\dot{\gamma}}{2} & 0 \end{bmatrix}. \tag{3}$$

The stress response, in rate form, at any point of the specimen can be obtained by the following assumed elastic isotropic constitutive law:

$$\dot{\boldsymbol{\sigma}}^{\mathrm{obj}} = \lambda \mathrm{tr}(\mathbf{D})\boldsymbol{\delta} + 2\mathrm{G}\mathbf{D} = 2\mathrm{G}\mathbf{D}\,, \tag{4}$$

where λ and G are the first and second Lamé constants, $\boldsymbol{\delta}$ is the 2nd-order identity tensor and $\dot{\boldsymbol{\sigma}}^{\mathrm{obj}}$ denotes any appropriate objective stress rate of the Cauchy stress $\boldsymbol{\sigma}$. In the present paper the following Cotter-Rivlin $\dot{\boldsymbol{\sigma}}^{\mathrm{CR}}$, Truesdell $\dot{\boldsymbol{\sigma}}^{\mathrm{TR}}$ and Jaumann-Zaremba $\dot{\boldsymbol{\sigma}}^{\mathrm{JZ}}$ objective stress rates are employed and their outcomes confronted:

$$\dot{\boldsymbol{\sigma}}^{\mathrm{CR}} = \dot{\boldsymbol{\sigma}} + \mathbf{L}^{\mathrm{T}} \cdot \boldsymbol{\sigma} + \boldsymbol{\sigma} \cdot \mathbf{L}\,, \tag{5}$$

$$\dot{\boldsymbol{\sigma}}^{\mathrm{Tr}} = \dot{\boldsymbol{\sigma}} - \mathbf{L} \cdot \boldsymbol{\sigma} - \boldsymbol{\sigma} \cdot \mathbf{L}^{\mathrm{T}} + \mathrm{tr}(\mathbf{L})\boldsymbol{\sigma}\,, \tag{6}$$

$$\dot{\boldsymbol{\sigma}}^{\mathrm{JZ}} = \dot{\boldsymbol{\sigma}} - \mathbf{W} \cdot \boldsymbol{\sigma} + \boldsymbol{\sigma} \cdot \mathbf{W}\,. \tag{7}$$

An ODE (Ordinary Differential Equation) system with solution for the Cauchy stress $\boldsymbol{\sigma}$ is obtained by putting objective stress rates (5)-(7) into the constitutive law (4), as showed in details in [1]. The corresponding analytical integration leads to the following expressions of the Cauchy stress $\boldsymbol{\sigma}$, according to the three assumed objective stress rates.

$$[\boldsymbol{\sigma}]^{\mathrm{CR}} = \begin{bmatrix} 0 & 0 & 0 \\ 0 & 0 & \dot{\gamma}\mathrm{Gt} \\ 0 & \dot{\gamma}\mathrm{Gt} & -\dot{\gamma}^2\mathrm{Gt}^2 \end{bmatrix}, \tag{8}$$

$$[\boldsymbol{\sigma}]^{\mathrm{Tr}} = \begin{bmatrix} 0 & 0 & 0 \\ 0 & \dot{\gamma}^2\mathrm{Gt}^2 & \dot{\gamma}\mathrm{Gt} \\ 0 & \dot{\gamma}\mathrm{Gt} & 0 \end{bmatrix}, \tag{9}$$

$$[\boldsymbol{\sigma}]^{\mathrm{JZ}} = \begin{bmatrix} 0 & 0 & 0 \\ 0 & \dot{\gamma}^2\mathrm{G}[\cos(\dot{\gamma}t) - 1] & \mathrm{G}\sin(\dot{\gamma}t) \\ 0 & \mathrm{G}\sin(\dot{\gamma}t) & \dot{\gamma}^2\mathrm{G}(1 - \cos(\dot{\gamma}t)) \end{bmatrix}. \tag{10}$$

The following graphs, reported in Fig. 1, present the analytical results in the form of three plots, namely the evaluated torque, outer shear stress and outer longitudinal stress vs. twist angle, by taking into consideration the same tubular specimen characteristics and the same torsion velocity as reported in [4]. The analysis is run up to 10 revolutions, i.e. 62.83 radiants, to evaluate the elastic response at large strains, for hypothetical illimited elastic behaviour (no material yielding). Similar trends stand as well for solid specimens, with results that differ only for the dissimilar internal radius. The results will be further commented in the Conclusions.

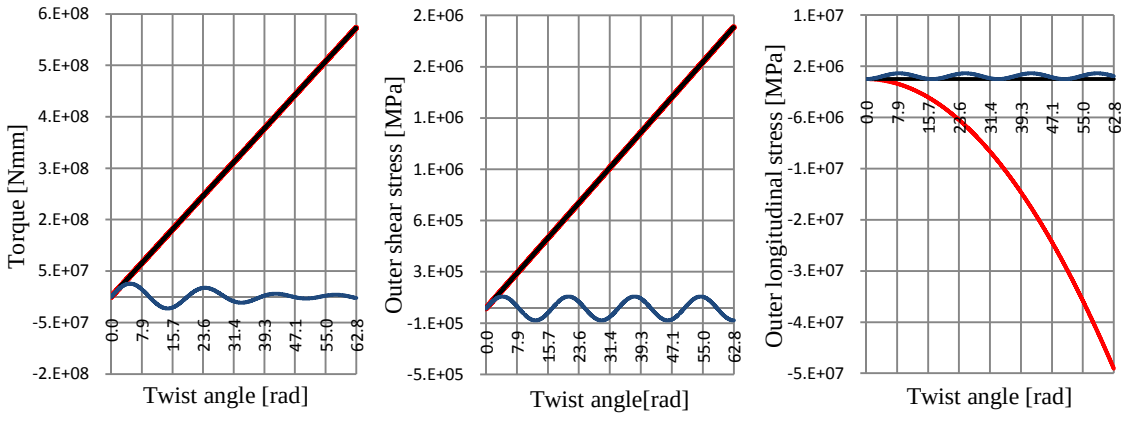

Figure 1. Analytical results for tubular specimens under fixed-end torsion: red curve for Cotter-Rivlin, black for Truesdell and blue for Jaumann-Zaremba stress rates.

NUMERICAL RESULTS

The numerical simulations are carried-out with 3D tetrahedral elements, using the Jaumann-Zaremba stress rate, according to an implementation that is available within the adopted FEM code (ABAQUS). Torsion is imposed to the FE specimen by means of two rigid studs, one fixed at one end and the other rotating at the other end with respect to the longitudinal axis of the specimen. The definition of a reference point for both studs makes easier the imposition of their motion, whether constraint or rotation must be imposed. Experimental observations in [4] determine that failure for tubular specimens manifests itself roughly at around 3.84 rad (220°) and for solid specimens at about 5 rad (287°). Thus, twist angles of 4.71 rad (270°) and 6.28 rad (360°) have been recognized as reasonable terms for the simulations in the two cases. The material properties adopted in the FEM models are derived by the tensile tests exposed in [4], for the AISI 1020 steel used therein. Same, all other characteristic parameters, such as specimen's geometrical properties and applied torsion velocity are taken from [4]. Worth-noting geometrical properties are the gauge length of 16 mm, for both specimens and the external radius of the gauge section, of 6 and 5 mm for tubular and solid specimens, respectively.

First, preliminary simulations have been carried-out to outline a coherent meshing procedure, with the goal of obtaining accurate-enough results at reasonable CPU time. The tubular specimen is discretised with 55643 elements and 12191 nodes, while the solid specimen, of smaller dimensions, is assembled with 33551 elements and 6601 nodes. Second, several hardening models have been investigated: 1) perfectly-plastic; 2) isotropic hardening; 3) linear kinematic hardening; 4) combined hardening (considering both isotropic and non-linear kinematic hardening); 5) combined hardening with damage and FE removal, to account for specimen's failure and consequent sudden torque drop. Thus, five different cases are examined for each condition, i.e. tubular vs. solid and free- vs. fixed-end. The implicit solver has been used for the first four hardening cases, whereas for the last case, which includes damage failure, the explicit solver has been employed. Carried-out preliminary simulations ensured that the implicit and explicit solvers were giving tight results, except for second-order oscillatory trends due to spurious dynamic effects that arise with the explicit solver. Following Figure 2 reports sample outcomes of the FE simulations for tubular specimens.

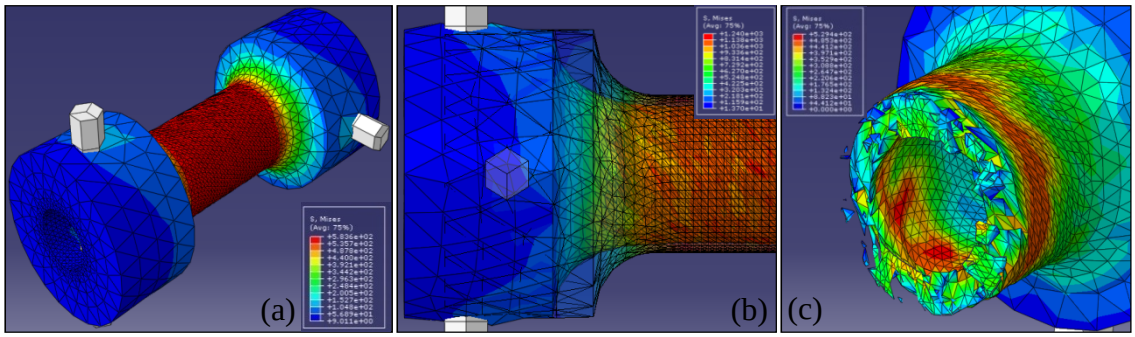

Figure 2. FE simulation of tubular specimens under free-end conditions: (a) Assembled model under torsion; (b) Swift effect; (c) Separation fracture.

Results for tubular specimens are presented in Fig. 3, by means of six graphs, taking into consideration both fixed- and free-end tests. The torque, axial force and axial elongation are evaluated at the reference point of the rotating stud, while the outer shear stress is evaluated as an average within two outer elements located in the center of the specimen. Different colours represent the five constitutive models taken into consideration: 1) red for perfectly-plastic; 2) blue for isotropic hardening; 3) orange for linear kinematic hardening; 4) green for combined hardening; 5) purple for combined hardening with damage. When experimental data from [4] are available, they are scored by a dotted black line; it must be remarked that these data always refer to fixed-end tests only.

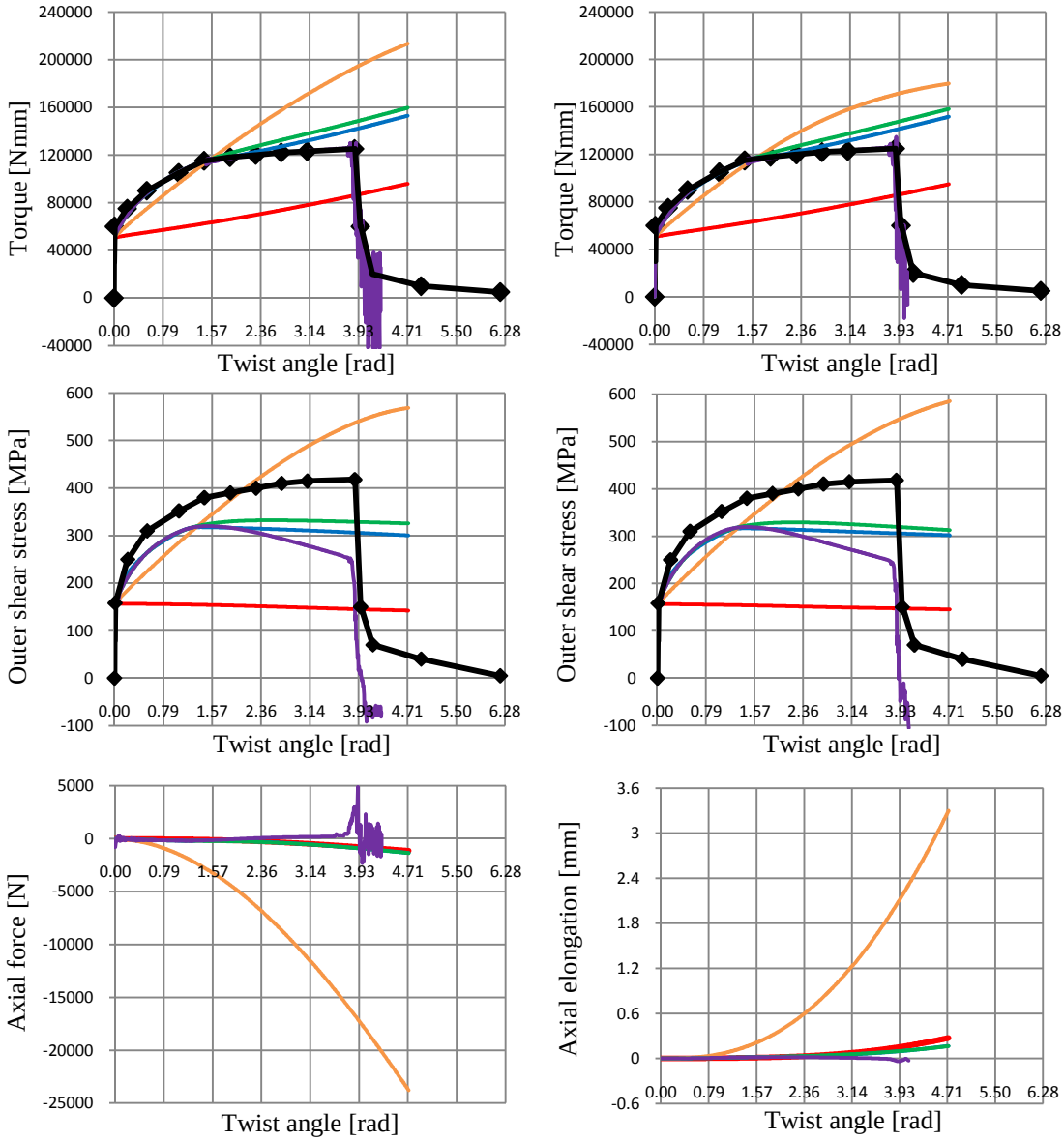

Figure 3. Numerical results for tubular specimens: fixed-end results in the left column; free-end results in the right column.

The same six graphs, in the same order but for solid specimens, are then presented in following Fig. 4.

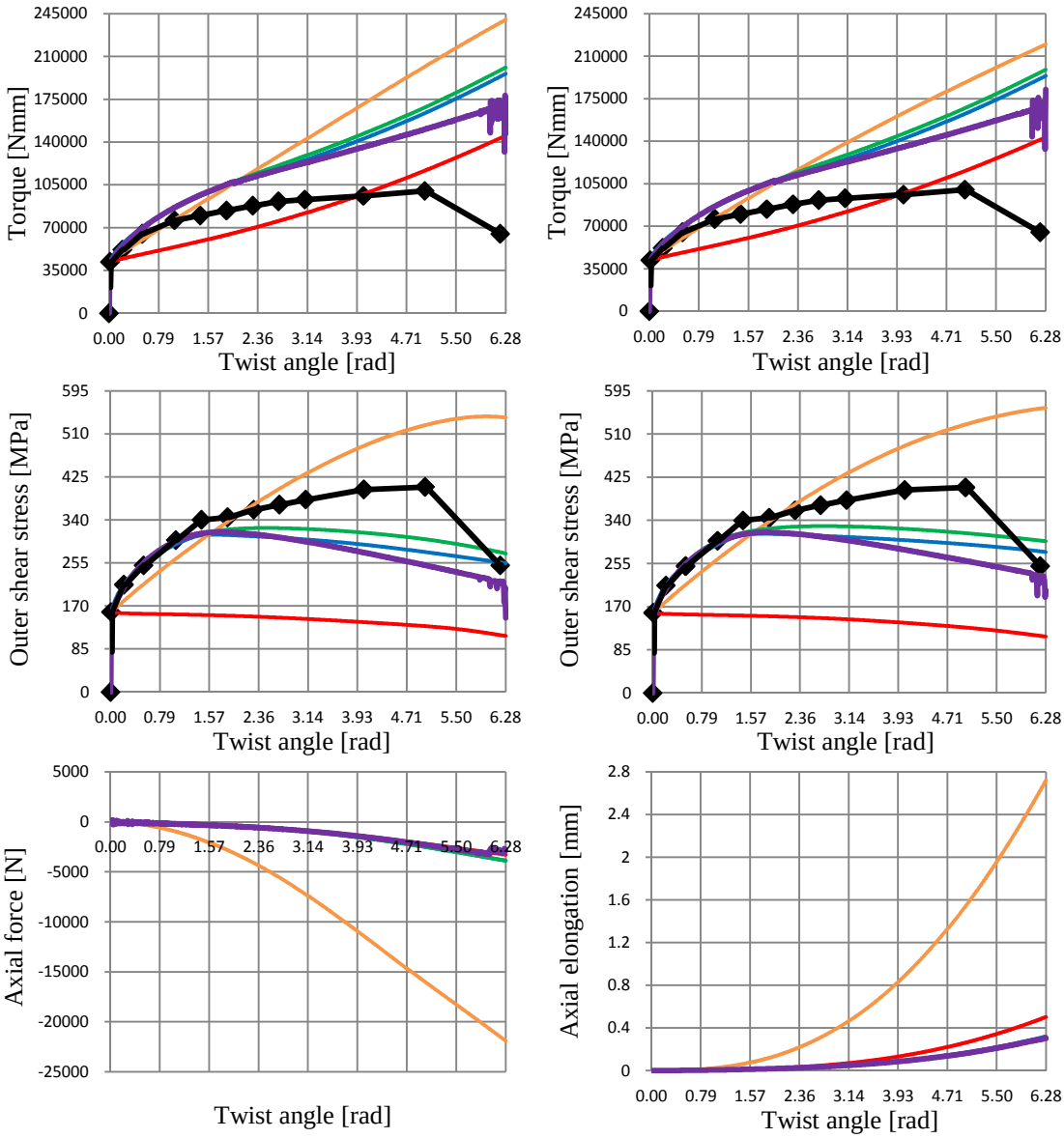

Figure 4. Numerical results for solid specimens: fixed-end results in the left column; free-end results in the right column.

Figure 5 presents a direct comparison between fixed- and free-end tests for tubular specimens, in terms of torque and outer shear stress vs. twist angle. It shows the small difference that appears between the two cases, which differ only for a little surplus of torque and shear stress for fixed-end results. Similar trends hold as well for solid specimens.

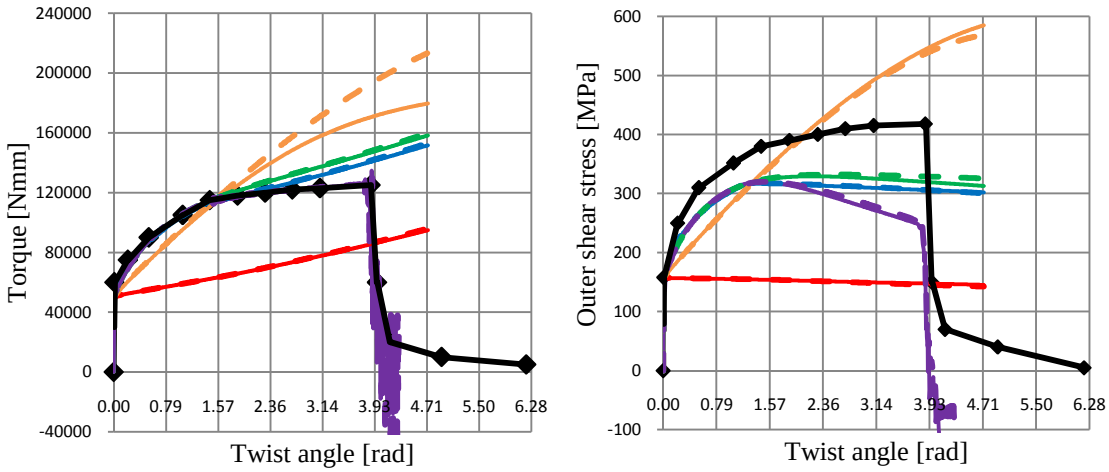

Figure 5. Direct comparison between fixed- (dotted lines) and free-end (solid lines) tests for tubular specimens.

Figure 6 presents a direct comparison between results for tubular and solid specimens in terms of axial force (for fixed-end tests) and axial elongation (for free-end tests) vs. twist angle, for the case of linear kinematic hardening, i.e. the one for which the Swift effect turns-out more susceptible. It shows clearly a strong difference between the two cases, with the tubular specimens that definitely display a higher Swift effect.

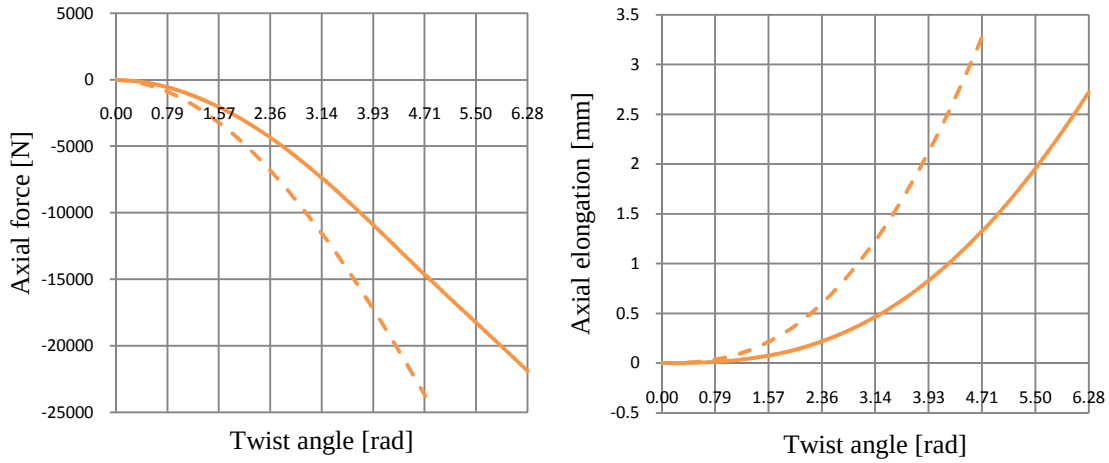

Figure 6. Swift effect outcomes for tubular (dotted lines) and solid (solid lines) specimens (linear kinematic hardening case).

CONCLUSIONS

From the analytical results it is possible to advance first important considerations on the validity of the three considered objective stress rates. The Cotter-Rivlin stress rate induces the presence of a shear stress component, linear with time and of a negative

(compression) longitudinal stress component, quadratic with time. The Truesdell stress rate implies the presence of the same previous shear stress component, but does not set a longitudinal stress component, while it determines instead a hoop stress component, positive and quadratic with time. The Jaumann-Zaremba stress rate outcomes in shear, longitudinal and hoop stress components but with oscillatory trends in time. This fact does not appear coherent with reality and seems to point-out the unsuitability of the Jaumann-Zaremba stress rate, at least in the examined elastic range. This confirms results obtained by different researchers under elastic simple shear, as cited in [1]. It can be concluded that the Cotter-Rivlin objective stress rate sets the best results, considering both shear and longitudinal stress components, while the Truesdell rate fails in setting a longitudinal stress component. Further, preliminary investigations under way show that the three objective stress rates behave differently in the elastoplastic range. In particular, the Jaumann-Zaremba objective stress rate does not set oscillatory trends in this case, for none of the three non-zero stress components.

Numerical results show a quite good correspondence in terms of the torque vs. twist angle response of the specimen, with case-to-case variations due to the different hardening model considered. In particular, the results for tubular specimens with combined hardening and damage reproduce almost perfectly the experimental data in [4]. It has to be emphasized that no explicit fitting attempts have been made here. The results are obtained merely by using the tensile data exposed in [4]. The only exception is for the damage model parameters, which have been suited to capture the breaking point of the experimental data for the tubular specimens. For what it concerns the Swift effect, it is interesting to note that it arises in all five examined cases, although with different magnitudes, which clearly state a sensitivity of the Swift effect on the assumed elastoplastic constitutive model.

On the base of the obtained analytical and numerical results, it seems reasonable to conclude that the Poynting/Swift effect manifests itself due to the finite strain kinematics of the torsion test, which determines the onset of a longitudinal stress component in the fixed-end test and of an axial elongation in the free-end test. This consideration confirms what is suggested by Billington in [3]. Moreover, the fact that the Swift effect arises for all five examined hardening cases could lead to think that further potential causes of its manifestation, like e.g. material anisotropy of the specimen, stress-induced anisotropy or hardening, may play a secondary role in this sense, acting more as magnitude parameters rather than causes.

REFERENCES

[1] Gambirasio, L., Chiodi, P. (2009) *"Simulazione numerica in deformazioni finite di provini metallici soggetti a torsione"*, Laurea Thesis, Advisor E. Rizzi, Università di Bergamo, Facoltà di Ingegneria (Dalmine), 512 pages.

[2] Swift, W. (1947) *Engineering*, **163**, 253–257.

[3] Billington, E.W. (1976) *Journal of Applied Physics*, **9**, 533–552.

[4] Bressan, J.D., Unfer, R.K. (2006) *J. of Materials Processing Technology*, **179**, 23–29.